

SCIENTIFIC REPORTS



OPEN

Temporally Resolved Intensity Contouring (TRIC) for characterization of the absolute spatio-temporal intensity distribution of a relativistic, femtosecond laser pulse

Daniel Haffa¹, Jianhui Bin ^{1,3}, Martin Speicher¹, Klaus Allinger¹, Jens Hartmann¹, Christian Kreuzer¹, Enrico Ridente^{1,2}, Tobias M. Ostermayr ^{1,2,3} & Jörg Schreiber ¹

Today's high-power laser systems are capable of reaching photon intensities up to $10^{22} \text{ W cm}^{-2}$, generating plasmas when interacting with material. The high intensity and ultrashort laser pulse duration (fs) make direct observation of plasma dynamics a challenging task. In the field of laser-plasma physics and especially for the acceleration of ions, the spatio-temporal intensity distribution is one of the most critical aspects. We describe a novel method based on a single-shot (i.e. single laser pulse) chirped probing scheme, taking nine sequential frames at frame rates up to THz. This technique, to which we refer as temporally resolved intensity contouring (TRIC) enables single-shot measurement of laser-plasma dynamics. Using TRIC, we demonstrate the reconstruction of the complete spatio-temporal intensity distribution of a high-power laser pulse in the focal plane at full pulse energy with sub-picosecond resolution.

Since the advent of chirped pulse amplification^{1,2} high-power laser systems have evolved and now enable novel particle acceleration techniques. Multi-GeV electrons³, x-rays⁴, neutrons⁵ and energetic ions^{6,7} emerge from intense laser-plasma interactions with targets. A milestone for acceleration of multi MeV ions has been demonstrated 2000⁸. Short acceleration lengths (MeV/ μm), small source sizes (μm), high particle flux^{9,10}, poly-energetic energy distributions and broad angular divergence¹¹ mark the key differences compared to the output from conventional accelerators. Substantial improvements of laser and target technology have enabled higher repetition rates also for solid targets^{12–16}. With the new generation of petawatt class laser systems^{17,18} proton energies up to 100 MeV¹⁹ in a single shot and repetition rates up to 1 Hz²⁰ at lower kinetic energies are now available, fueling enthusiasm on the way to developing laser-driven systems¹¹.

Two of the most influential aspects relevant to laser-ion acceleration are the temporally resolved intensity contrast²¹ and the transverse intensity distribution in the focal plane. Due to sub-picosecond duration and the high peak intensity a direct measurement of such remains challenging. In fact the spatial and temporal intensity distributions are often determined independently, for separate shots and with attenuated beams. The temporal intensity contrast is typically measured relatively (in relation to the peak intensity) with autocorrelation methods^{22,23} which integrate over the spatial distribution. Newest approaches aiming for single-shot measurements^{24,25} seem very promising for monitoring the temporal shape of the intensity during the interaction. The spatial intensity distribution is usually measured with time-integrating beam profilers using an attenuated laser pulse and

¹Lehrstuhl für Medizinphysik, Fakultät für Physik, Ludwig-Maximilians-Universität München, 85748, Garching b. München, Germany. ²Max-Planck-Institut für Quantenoptik, 85748, Garching b. München, Germany. ³Accelerator Technology and Applied Physics Division, Lawrence Berkeley National Laboratory, Berkeley, CA, 94720, USA. Correspondence and requests for materials should be addressed to D.H. (email: Daniel.Haffa@physik.lmu.de) or J.H.B. (email: jianhuibin@lbl.gov) or M.S. (email: Martin.Speicher@physik.lmu.de)

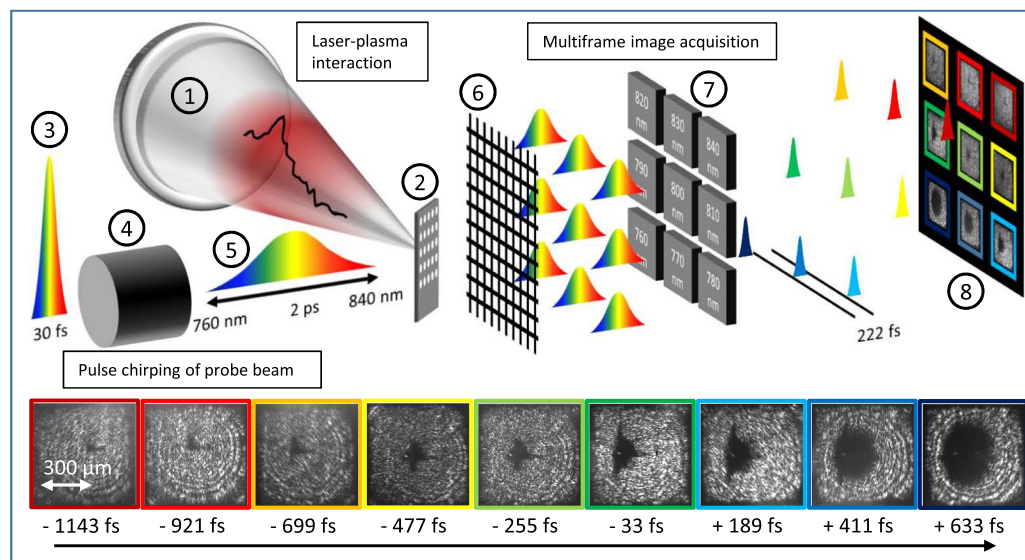


Figure 1. Experimental Setup for TRIC. A Ti:Sapphire laser pulse (1) is focused onto a 200 nm thick Formvar target (2) at 45° incidence. A small part of the short laser pulse is coupled out earlier (3) and sent through a glass rod (4). The emerging chirped pulse (5) passes the target perpendicularly to the main pulse. In the imaging path, the probe beam is multiplied using a low dispersion transmission grating (6). A small frequency range is cut out of each of the replicas by narrow bandpass filters (7) before being recorded with a camera (8). The bottom row shows a sample picture series recorded in a single-shot.

the anticipated high intensities require mapping with high dynamic range (at least five orders of magnitude) in order to avoid an overestimation of the peak intensity at focus²⁶. Also several methods have been developed to measure the peak intensity of high-power laser pulses^{27–29}. A combined spatio-temporal measurement of an attenuated high-power laser focus has recently been demonstrated for the first time³⁰. Although several techniques allow the analysis of the spatial and temporal intensity distribution of a high-power laser focus^{22–26,31,32}, it has not been directly accessible during a laser-plasma interaction. Here we describe a technique that measures the spatio-temporal evolution of a laser-induced plasma on target for a single-shot. This not only yields information about the evolution of plasma formation, but can be further interpreted to retrieve the absolute spatio-temporal intensity distribution (STID) of a high-power laser in the focal plane at full intensity. Within a single-shot we measure temporally resolved intensity contours with sub-picosecond temporal resolution and about 25 μm spatial resolution. With each additional measurement with modified laser intensity (in our example five pulses) we add about one order of magnitude to the covered dynamic range of our measurement. Because there are no direct comparisons with our novel technique, we extract the transverse spatial and the temporal profiles of the three-dimensional intensity distribution function, and compare them to the standard techniques, i.e. a spatial high dynamic range (HDR) focus image (integrated over the full laser pulse duration) and a temporal contrast measurement taken with a third-order autocorrelator.

Experimental Setups

The experimental setup resembles a typical pump-probe configuration and is shown in Fig. 1. The Ti:Sapphire system provides 374 mJ on target within 30 fs with a spectral range of 760 nm to 840 nm. The laser is focused onto a 200 nm thick Formvar foil target¹⁵ with a diameter of 2 mm which is positioned for irradiation at 45 degree incidence. A small fraction of the 30 fs laser beam is coupled out in advance to provide the probe beam. After traversing a glass rod, the resulting chirped probe pulse of 2 ps duration is overlapped perpendicularly with the main laser pulse at the target. The transmitted probe light is collected with a lens, guided from the vacuum chamber and imaged with another lens onto a camera (Prosilica GT 4907, Allied Vision) with a magnification of ≈ 6.5 and a spatial resolution of roughly 1.5 μm. A 2D grating (Collischon, 15 μm lattice constant) is positioned between the lens and the CCD chip, such that nine spatially separated replicated images are accommodated on the camera chip. Each image still contains the complete spectrum. By adding nine different narrow band-pass filters (bandwidth of 10 nm) in front of the camera chip at the positions of the replicas they will be spectrally filtered and thus correlated temporal information is imprinted^{33,34} onto each image. The time delay between subsequent images is defined by the set spectral chirp and in our case set to 222 fs (see methods). We thus measure nine sequenced images with a frame rate of 5 THz, revealing the plasma evolution in response to a high-power laser pulse interacting with a solid density target. It is worth mentioning, that this implementation can considerably simplify single-shot probe schemes that have been realized in the past^{35–38}. An exemplary raw image of such measurement is displayed in Fig. 1. The image appears bright in areas where the target remains transparent and dark in areas, where the target became opaque. The cause for this binary image information is the change in the optical transmission of the evolving plasma. When the free electron density becomes larger than the critical density $n_e > n_c$,

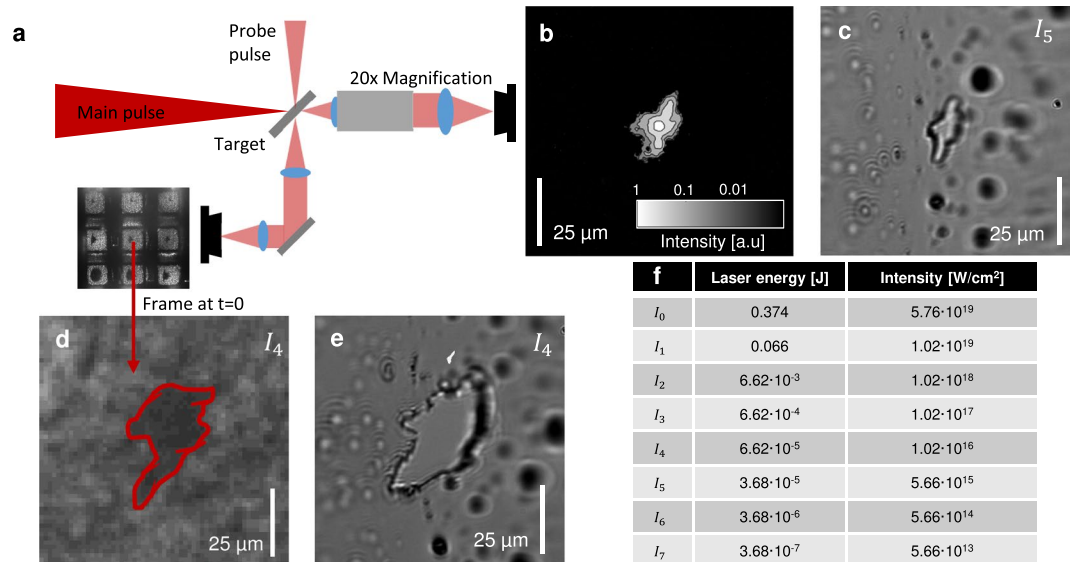


Figure 2. Nexus of intensity distribution and plasma shape. This figure shows separately obtained images of the laser focus, the probe image and the hole in the target after the shot. The configuration can be seen in (a), a 20 times magnifying microscope views the target under an angle of 45° and also measures an attenuated pulse in the focal plane (b) (contour image). The hole in the target with intensity I_5 is shown in (c). A shot with intensity I_4 compares the hole in the target (e) to the probe image (d). The table (f) lists the laser energies on target and corresponding intensities used during the experiment.

the plasma turns reflective for the incoming probe pulse. The horizontal dimension recorded in the image contains convoluted information since the laser and the orthogonal probe pulse both hit the target under an angle of 45° . The probe image is thus a projection. At the same time, the orientation of the target with respect to the drive beam implies that non-central parts of the target interact with the laser in out-of-focus planes causing a complex two-fold convolution of time and space. A spatial difference in horizontal dimension of $60 \mu\text{m}$ in the image, corresponds to a time difference of 200 fs of both the laser and probe pulse hitting the target. For simplicity we therefore only consider the vertical dimension, where those effects do not play a role.

Relation of Laser Intensity and Plasma Contour

The measured average growth of the overdense plasma area (dark region) of the single-shot image sequence in Fig. 1 is evaluated to be about 30% of the speed of light. The first step was to examine the source for this plasma expansion in more detail.

We therefore varied the laser intensity and compared the spatial intensity distribution of the laser focus with the contour of the overdense plasma during the interaction and the hole at the target long time after each shot. The laser energy was reduced by adding neutral density filters in the beam path of the laser before compression and thus attenuating both the main pulse and the probe pulse. The corresponding intensities are shown in Fig. 2f. The hole in the target after the shot with intensity I_5 is shown in Fig. 2c. Since the angle of the target was 45° with respect to the laser axis and thus also to the microscope (Fig. 2a), only the central vertical axis appears sharp. Comparison to a contour plot of the laser focus, taken with an attenuated beam (Fig. 2b), indicates great resemblance. The picture was taken with the same microscope. Comparison of the laser intensity profile (Fig. 2b) and the hole in the target after the shot (Fig. 2c) indicates the contour of the hole to be directly correlated to the shape of the laser focus at a certain intensity. The distortion of the laser focus makes this effect more clear. In Fig. 2d we see the measured plasma shape with the probing technique at $t=0$ (largest contour) with an intensity of I_4 of the main pulse. The hole in the target foil after the shot is shown in Fig. 2e and again the contours in Fig. 2d,e show excellent resemblance. This indicates that the threshold intensity, where the Formvar target becomes opaque and thus $n_e \geq n_c$ can be related to the contour of the hole in the target after the shot. As a conclusion of this empirical observation we state, that the intensity at the measured contour of the plasma is the isosurface of the intensity distribution of the laser focus reaching a certain threshold intensity. This threshold $I_{\text{th}} = (6 \pm 5) \cdot 10^{13} \cdot \text{W cm}^{-2}$ was determined by reducing the laser energy stepwise and thus the intensity until no hole was observed at the target after the shot (see methods). In the previous part we have simplified a few physical aspects. This is mostly valid since the threshold intensity ($I_{\text{th}} = (6 \pm 5) \cdot 10^{13} \cdot \text{W cm}^{-2}$) is significantly lower than relativistic intensities $\approx 10^{18} \cdot \text{W cm}^{-2}$, where other effects such as relativistic transparency³⁹, relativistic self-focusing⁴⁰ and self-phase-modulation⁴¹ can play a role. We further assume, that the enlargement of the plasma is caused, when the intensity distribution of the laser pulse reaches the threshold intensity and the target is ionized to reach free electron density beyond the critical density $n_e \geq n_c$. Another cause of an advancing plasma diameter could be the transverse expansion of the plasma itself by hot electrons^{42,43}. In the center of the laser focus at $t=0$ the laser eventually reaches relativistic intensities for the shots with highest laser energy and thus in the inner part relativistic transparency, self-focusing and other effects can play a significant role. Also the electron temperature at the central part of the laser focus can be beyond the MeV level, resulting in expansion

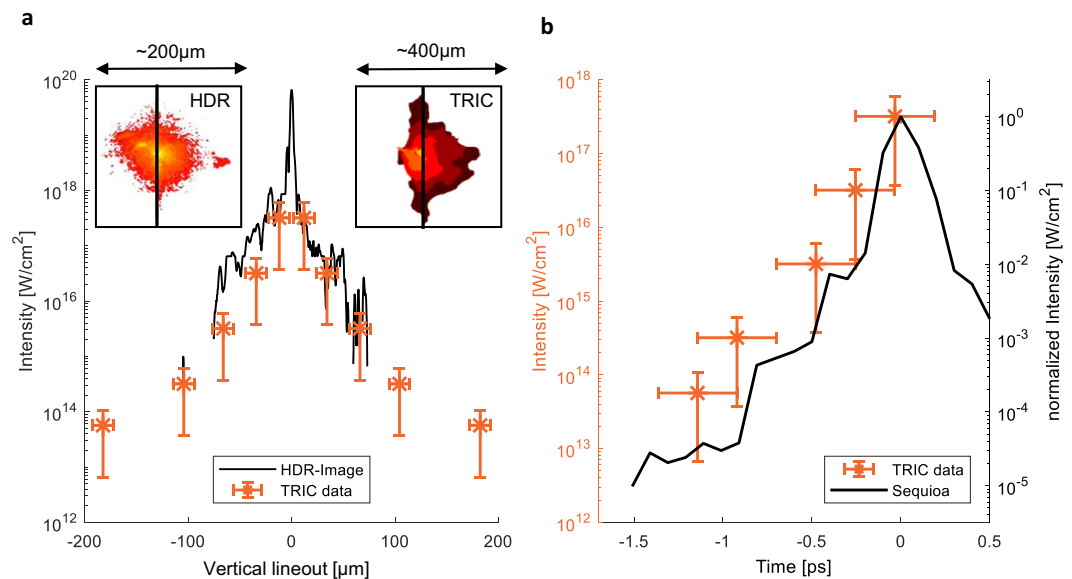


Figure 4. Comparison of TRIC to contrast curve and HDR focus image. **(a)** Compares the intensity distribution measured with TRIC and with a HDR camera. Line-outs of the HDR focus (left inset) and the TRIC focus (right inset) are shown. **(b)** Shows the temporal contrast of TRIC at $x = 0 \mu\text{m}$ and $y = 15 \mu\text{m}$. For comparison the right axis shows a normalization compared to the measurement taken with the Sequoia-autocorrelator.

$$I_{\text{seci}}(x, y, t) = I_{\text{th}} \cdot C_i. \quad (2)$$

Repeating this for several C_i yields the absolute spatio-temporal intensity map as shown in Fig. 3. Each row corresponds to a single-shot with different attenuation coefficient and thus the scaled contour corresponds to a different intensity I_{seci} . The summation over those measurements enables the retrieval of the absolute spatial intensity distribution of the laser focus at distinct time steps and is shown in Fig. 3b. Figure 3b is thus the complete STID of a high-power laser pulse in the focal plane, measured at full pulse energy on target and represents our main result. We note that the horizontal dimension is still temporally blurred due to the chosen probing geometry as described before. For further comparison a line-out at $x = 0 \mu\text{m}$ (central vertical line) is used. The intensity map features measuring the spatial intensity profiles at select time steps and reveals the temporal dynamics at a given position. The most interesting cases are the spatial distribution of the peak intensity ($t = 0$) and the temporal contrast at the central point ($x = 0$ and $y = 0$). We therefore evaluated $I(x, y, t = 189 \text{ fs})$ as displayed in Fig. 4a, since it was the closest time step past the interaction with the peak of the main pulse ($t = 0$) and $I(x = 0 \mu\text{m}, y = 15 \mu\text{m}, t)$ as displayed in Fig. 4b. Due to its current form limited spatial resolution we could not resolve the central area $< 25 \mu\text{m}$. Therefore the most intense measured contour represents $3.18 \cdot 10^{17} \cdot \text{W cm}^{-2}$, which is orders of magnitude below the classically estimated peak intensity of $5.76 \cdot 10^{19} \cdot \text{W cm}^{-2}$.

Comparison to contrast curve and laser focus. To assess our method we compared the extracted temporal and spatial intensity distribution to data obtained by conventional methods, a contrast profile of a third-order autocorrelator (averaged over a small portion of the collimated beam - no spatial information) $g(t)$ and a HDR image of the laser in the focal plane (integrated over time) $f(x, y)$ ²⁶. Both of those standard measurements yield only relative information, which we scale to absolute values by calculating

$$I(x, y, t) = E_{\text{Laser}} \cdot f(x, y) \cdot g(t), \quad (3)$$

where $E_{\text{Laser}} = 374 \text{ mJ}$ is the full laser pulse energy measured for each shot (see methods). The spatial shape function of the laser focus $f(x, y)$ and the temporal laser contrast-curve $g(t)$ are both normalized, $\int f(x, y) dx dy = 1$ and $\int g(t) dt = 1$. Note that this separation of the temporal and spatial profiles neglects effects of spatio-temporal coupling⁴⁴ by definition.

HDR focus picture. The HDR focus image is the integrated spatial distribution over the full duration of the laser pulse and can thus be normalized to $f(x, y)$. Assuming a Gaussian profile for the temporal distribution of the laser pulse, with a full-width at half-maximum $\tau_{\text{FWHM}} = 30 \text{ fs}$ (laser pulse duration), the spatial intensity distribution of a measured HDR laser focus at time $t = 0$ is

$$I(x, y, t = 0) = E_{\text{Laser}} \cdot f(x, y) \cdot \frac{1}{\sqrt{2\pi}\sigma}, \quad (4)$$

with $\sigma = \frac{\tau_{\text{FWHM}}}{2.35}$.

Figure 4a compares a line-out of this function along the vertical dimension (at $x=0$) with the result obtained by TRIC at $t=189$ fs. The focus, measured offline with the camera, appears continuous since it has more data points, while TRIC contributes a small number of points (dictated by the number of shots with different attenuation coefficients). In the overlap region, both methods yield similar comparable results. With TRIC we can measure down to I_{th} , which exceeds the capability of HDR imaging as this is limited by damage of the camera. With an increased spatial resolution of TRIC, we expect to resolve also the peak of the pulse such that a 7 orders of magnitude dynamic range seems feasible. The horizontal error bar originates from the readout of the diameter of the contour. The rather large error bar for the evaluated intensities is due to the error of the determination in the threshold intensity.

The temporal intensity distribution. The Sequoia is a scanning third order autocorrelator and measures the temporal intensity contrast relative to the laser peak. Comparison to the absolute temporal intensity evolution at a fixed spatial position, as accessible with TRIC, requires more assumptions. We thus solely compare the autocorrelator contrast curve to a normalized curve measured with TRIC as indicated in Fig. 4b (right axis). We normalized both intensities such that the peak ($t=0$) is equal to one. The extent of temporal error bars of TRIC is attributed to the time interval correlated to the width of the bandpass filters for each time step in addition to an increment from time delay uncertainty. The intensity error bars originate from the uncertainty of the determined damage threshold. The TRIC values follow the shape of the autocorrelation trace but indicate reduced temporal contrast. The reason for this disagreement between the autocorrelation trace and the trace extracted from TRIC is not clear but one of the interesting features that can be studied with TRIC. Spatio-temporal coupling⁴⁴, which can have diverse origins, manifests in focus (the simplest example is pulse lengthening by a pulse front tilt). This is where TRIC can yield complementary information. It highlights the necessity of monitoring and controlling the laser contrast on target at full energy, especially in the focal plane. More detailed measurements with an improved spatial resolution will help to shed light on this interesting aspect.

Summary and Discussion

By using a simple method of beam multiplexing we enable recording of nine images of the plasma evolution during the interaction of a high-power laser pulse with a thin solid density target in a single-shot. Our interpretation of the such obtained images in the framework of TRIC yields information about the absolute STID in the focus of a high-power laser pulse. We note though, that if the spatial intensity distribution on target was significantly steeper, for example in the case of a perfect Gaussian pulse, this interpretation can be misleading and the transversely streaming electrons could contribute or even dominate the observed expansion front. Determining the STID in focus at high peak intensity is specially interesting in combination with plasma mirrors¹⁶ or other non-linear techniques⁴⁵ that aim to manipulate the laser pulse close to target. TRIC gives access to the spatial intensity distribution at energies slightly above I_{th} . We note that it requires still analytical effort to account for the horizontal dimension. Because the ignition of the plasma and thus the change of opacity is irreversible on ultra-fast timescales, TRIC only yields information of the rising slope of the laser pulse and therefore requires the assumption of an intensity distribution that rises monotonically over time. Two short prepulses with intensities around $10^{14} \cdot W \text{ cm}^{-2}$ and thus just above the threshold intensity occurring ≈ 600 ps prior to the main pulse have been identified in the laser-system using third-order autocorrelation. If they were focused to a similar spot as the main pulse, they would have reached $10^{14} \cdot W \text{ cm}^{-2}$ for the shots with highest energy of 374 mJ. Although exceeding the intensity threshold for TRIC, we have not observed a respective contour when probing at times as early as 100 ps before the main pulse. We note though, that the contour with a size of a few μm could have not been detected with TRIC in its current spatial resolution limit. The absence of any sign of target damage/modification due to these prepulses on the other hand reconfirms that the measurement is not disturbed by transverse plasma-expansion initiated by very early prepulses at sufficiently low intensity, since no plasma shape is recorded in the probe beam until 1.3 ps prior to the peak of the pulse as evidenced in the last line of Fig. 3. It remains important to keep in mind such potential sources of miss-interpretation though. For example when prepulses have much higher intensity such pre-expansion can cause a plasma that indeed expands and mimics a contour that is not related to the intensity contour any longer. Such prepulses, however, would be easily identified in autocorrelation measurements and would not require TRIC. Additional uncertainties can be caused by absorption or divergence of the probe pulse in the plasma. However, the close resemblance between the contour of the hole and the plasma shape that we observed, does not indicate that this is relevant for extracting the contour lines from the images. Improving this resolution to a few μm will increase the sensitivity to prepulses just above the I_{th} . A more detailed determination of the threshold intensity would further allow a reduction of this systematic error and thus an even more accurate determination of the absolute intensity distribution on target.

The technique of acquiring multiple images by exploiting the natural features of a broadband highly intense laser-pulse, can be adapted to other, more complicated probing techniques, e.g. using holography^{46,47} instead of binary shadowgraphy. It can therefore add a temporal component to diverse probing experiments. Thus, we see TRIC as a very first step that is accessible with this technique. In the future we foresee a potential use of TRIC for different pump-probe modalities. Especially the intrinsic synchronization in laser-driven particle acceleration processes enables temporal resolved investigations of the interaction of ions, electrons and x-rays with matter. The demonstrated sub-ps temporal resolution could for example also be exploited further for development of a time-of-flight measurement^{48,49} of ion bunches with combined temporal and 2D spatial resolution.

Methods

The ATLAS-300 is a single CPA laser system based on a Titanium Sapphire system and can be operated at a 5 Hz repetition rate. The pulse length of 30 fs is measured with FROG³¹ and the temporal contrast was measured with a third-order autocorrelator (Sequoia or Tundra). Several Pockels cells are implemented in the system to clean the ns contrast, the fastest one has a rise time of about 500 ps. The temporal laser contrast has been found to be in

the order or 10^{-9} from a few ns up to shortly before the main pulse ≈ 50 ps measured over 2 ns prior to the main pulse. Two short prepulses with $\approx 10^{-6}$ of peak power have been identified about 600 ps prior to the main pulse, originating from reflections in the regenerative amplifier. Further measurements with saturated photodiodes have not shown any significant prepulses in the ns range prior to the pulse. Therefore the majority of the energy is in the main pulse and the measured energy (determined with an energy meter) is used for calculations of the focus intensity. To monitor the energy of each shot a second energy meter is positioned behind a leakage mirror close to the experiment. At lower energies the sensitivity of the energy meter was not sufficient. In this case, the energy was estimated by integrating over the spectrum measured with an Ocean Optics spectrometer for each shot. The neutral density filters that are used to attenuate the beam during the experiment are positioned in the stretched beam before the compressor (≈ 400 ps). The probe beam is coupled out by a pickoff mirror about 2 meters before the laser-target interaction at the edge of the beam. The main laser is focused with a 90° , $f=2$ silver parabola with 20 cm focal length impinging onto target with p-polarization. The resulting HDR focus picture is depicted in Fig. 3 with a resulting FWHM of about $3 \mu\text{m}$. The HDR image of this time-integrated focal spot distribution provides the basis for calculating the peak intensity²⁶.

The probe pulse was coupled out with a pick off mirror at the edge of the main laser pulse in the target chamber (spatial sampling). The timing of the probe beam with respect to the main laser pulse was controlled with a delay stage. The probe beam was then guided through an aperture of 7.5 mm diameter. This aperture was imaged onto the interaction point (IP) with a demagnification of 9, resulting in an illuminated area of $\approx 830 \mu\text{m}$. A glass rod of 3 cm length was introduced in the beam path prior to target in order to chirp the pulse up to 2 ps. The energy of the probe beam was $\approx 0.5\%$ of the energy of the main pulse, resulting in a maximum of 20 mJ and an intensity of $1 \cdot 10^{12} \cdot \text{W cm}^{-2}$ on target. The intensity of the probe was thus 5 orders of magnitude lower than the intensity of the main pulse and further distinctly smaller than the threshold intensity. Due to the modified energy of the laser and thus also the probe beam, it was further filtered in front of the camera (for high energies). An intended good contrast between the image created by the probe and self-emission from the target favored filtering in front of the camera instead of filtering prior to the target. The imaging system of the probe beam was based on a two-lens-system resulting in a magnification of the probe image (in focal plane) of ≈ 6.5 . The first lens (2 inch) with a focal length of 10 cm is used to collect the light so it can thus further be guided out of the vacuum chamber. A second lens is used to image the IP onto the camera. A transmission grating (Collischon, $15 \mu\text{m}$ lattice constant) is placed in the beam path of the second lens to the camera, creating 9 nearly identical replicas on the camera chip. The narrow bandpass (10 nm FWHM) filters with dimensions $5 \times 5 \cdot \text{mm}^{-2}$ (Omega Optical Inc.) are placed directly in front of the camera chip. The spatial resolution of the complete setup was determined experimentally to about $25 \mu\text{m}$. This is significantly lower than the theoretical resolution of the imaging system, which would support $\approx 2 \mu\text{m}$ (Abbe limit). The main limiting factor is the low quality of the beam profile of the probe beam, which shows strong intensity fluctuations on the order of $10 \mu\text{m}$ spatial scale.

The zero timing describes the coincidence of the incident of probe and main pulse on the target. It was measured with the use of an air plasma ignited by the attenuated pump pulse in air. A high-power laser pulse can generate an air plasma when a certain intensity threshold⁵⁰ is reached. Therefore the laser intensity was diminished until the air plasma was solely visible in one or two of the nine frames and therefore marking the peak of the laser pulse with an accuracy of ± 222 fs. It should be noted that the probe beam is coupled out in the vacuum chamber and has thus also been in air for the determination of the zero timing.

The frame rate of the camera is set by the temporal spacing of the spectral images and the chirp of the probe pulse. Therefore the group velocity dispersion has to be calculated including complete knowledge of the stretching material in the probe beam and respective material characteristics. Since multiple error sources are introduced, we chose a different approach. Two nine-frame images are created, differing in delay by 1000 steps of the motor of the delay stage. If a specific plasma size is observed in two different frames of both nine-frame images, one can check for the change in the frame number and unambiguously correlate frame-number and temporal delay. Knowing that 1000 steps equal a delay of 666 fs the frame rate can be simply calculated. In the setup described above, a 3 cm glass rod resulted in a delay of 222 fs between each frame and a total observation time of 2 ps within a single-shot.

The threshold intensity was determined by focusing the main laser pulse onto a 200 nm thick plastic foil with a peak intensity that was calculated via equation 4. The target was examined after the shot with a 20 times magnifying microscope in the vacuum chamber. By reducing the intensity stepwise according to the values given in Fig. 2 we identified that the target had no visible hole after a single-shot with peak intensity $I_7 = 5.77 \cdot 10^{13} \cdot \text{W cm}^{-2}$, whereas a clear hole was visible after a shot with I_6 . We thus, supported by the extensions of the hole in the target after one shot with I_6 , determined the threshold intensity of the 200 nm plastic target to be $I_{\text{th}} = (6 \pm 5) \cdot 10^{13} \cdot \text{W cm}^{-2}$. We further note, that we empirically found that the intensity, needed to create an overdense and thus opaque plasma, also caused a hole in the target. The laser-induced damage threshold of different materials has been discussed widely over the last decades. The correlation between the conduction band (free) electron density reaching the critical density and damage due to ablation, is broadly accepted^{51,52}. However, newer research indicates that higher electron densities are required until damage occurs^{33,54}. Because we only use the transition from transparent to opaque for determining the contours, which happens for any free electron density $n_e \geq n_c$, our method is not sensitive to the exact damage mechanism. The threshold intensity $I_{\text{th}} = (6 \pm 5) \cdot 10^{13} \cdot \text{W cm}^{-2}$ should therefore not be associated with a damage threshold. Note, that the large error bar of I_{th} results from the course intensity filtering steps.

Data Availability

The datasets generated during and/or analyzed during the current study are available from the corresponding author on reasonable request.

References

1. Strickland, D. & Mourou, G. Compression of amplified chirped optical pulses. *Optics Communications* **56**, 219–221 (1985).
2. Maine, P., Strickland, D., Bado, P., Pessot, M. & Mourou, G. Generation of ultrahigh peak power pulses by chirped pulse amplification. *IEEE Journal of Quantum Electronics* **24**, 398–403 (1988).
3. Esarey, E., Schroeder, C. B. & Leemans, W. P. Physics of laser-driven plasma-based electron accelerators. *Reviews of Modern Physics* **81**, 1229–1285 (2009).
4. Khrennikov, K. *et al.* Tunable All-Optical Quasimonochromatic Thomson X-Ray Source in the Nonlinear Regime. *Physical Review Letters* **114** (2015).
5. Roth, M. *et al.* Bright Laser-Driven Neutron Source Based on the Relativistic Transparency of Solids. *Physical Review Letters* **110** (2013).
6. Kim, I. J. *et al.* Radiation pressure acceleration of protons to 93 MeV with circularly polarized petawatt laser pulses. *Physics of Plasmas* **23**, 070701 (2016).
7. Wagner, F. *et al.* Maximum Proton Energy above 85 MeV from the Relativistic Interaction of Laser Pulses with Micrometer Thick CH₂ Targets. *Physical Review Letters* **116** (2016).
8. Snavely, R. A. *et al.* Intense high-energy proton beams from petawatt-laser irradiation of solids. *Physical Review Letters* **85**, 2945 (2000).
9. Daido, H., Nishiuchi, M. & Pirozhkov, A. S. Review of laser-driven ion sources and their applications. *Reports on Progress in Physics* **75**, 056401 (2012).
10. Macchi, A., Borghesi, M. & Passoni, M. Ion acceleration by superintense laser-plasma interaction. *Reviews of Modern Physics* **85**, 751–793 (2013).
11. Schreiber, J., Bolton, P. R. & Parodi, K. Invited Review Article: “Hands-on” laser-driven ion acceleration: A primer for laser-driven source development and potential applications. *Review of Scientific Instruments* **87**, 071101 (2016).
12. Borot, A. *et al.* High-harmonic generation from plasma mirrors at kilohertz repetition rate. *Optics Letters* **36**, 1461 (2011).
13. Spindloe, C. *et al.* High volume fabrication of laser targets using MEMS techniques. *Journal of Physics: Conference Series* **713**, 012002 (2016).
14. Poole, P. L. *et al.* Liquid crystal films as on-demand, variable thickness (50–5000 nm) targets for intense lasers. *Physics of Plasmas* **21**, 063109 (2014).
15. Seuferling, S. *et al.* Efficient offline production of freestanding thin plastic foils for laser-driven ion sources. *High Power Laser Science and Engineering* **5** (2017).
16. Obst, L. *et al.* Efficient laser-driven proton acceleration from cylindrical and planar cryogenic hydrogen jets. *Scientific Reports* **7** (2017).
17. Papadopoulos, D. *et al.* The Apollon 10 PW laser: Experimental and theoretical investigation of the temporal characteristics. *High Power Laser Science and Engineering* **4** (2016).
18. CALA - Centre for Advanced Laser Applications: Mainpage, <https://www.cala-laser.de/>.
19. Higginson, A. *et al.* Near-100 MeV protons via a laser-driven transparency-enhanced hybrid acceleration scheme. *Nature Communications* **9** (2018).
20. Gao, Y. *et al.* An automated, 0.5 Hz nano-foil target positioning system for intense laser plasma experiments. *High Power Laser Science and Engineering* **5** (2017).
21. McKenna, P. *et al.* High-intensity laser-driven proton acceleration: Influence of pulse contrast. *Philosophical Transactions of the Royal Society A: Mathematical, Physical and Engineering Sciences* **364**, 711–723 (2006).
22. Blount, E. I. & Klauder, J. R. Recovery of Laser Intensity from Correlation Data. *Journal of Applied Physics* **40**, 2874–2875 (1969).
23. Luan, S., Hutchinson, M. H. R., Smith, R. A. & Zhou, F. High dynamic range third-order correlation measurement of picosecond laser pulse shapes. *Measurement Science and Technology* **4**, 1426–1429 (1993).
24. Wang, Y. *et al.* Single-shot measurement of >1010 pulse contrast for ultra-high peak-power lasers. *Scientific Reports* **4** (2015).
25. Oksenhendler, T., Bizouard, P., Albert, O., Bock, S. & Schramm, U. High dynamic, high resolution and wide range single shot temporal pulse contrast measurement. *Optics Express* **25**, 12588 (2017).
26. Hartmann, J. *et al.* The spatial contrast challenge for intense laser-plasma experiments. *Journal of Physics: Conference Series* **1079**, 012003 (2018).
27. Poder, K. *et al.* Experimental Signatures of the Quantum Nature of Radiation Reaction in the Field of an Ultraintense Laser. *Physical Review X* **8** (2018).
28. Link, A. *et al.* Development of an *in situ* peak intensity measurement method for ultraintense single shot laser-plasma experiments at the Sandia Z petawatt facility. *Review of Scientific Instruments* **77**, 10E723 (2006).
29. Har-Shemesh, O. & Di Piazza, A. Peak intensity measurement of relativistic lasers via nonlinear Thomson scattering. *Optics Letters* **37**, 1352 (2012).
30. Pariente, G., Gallet, V., Borot, A., Gobert, O. & Quéré, F. Space–time characterization of ultra-intense femtosecond laser beams. *Nature Photonics* **10**, 547–553 (2016).
31. Trebino, R. *et al.* Measuring ultrashort laser pulses in the time-frequency domain using frequency-resolved optical gating. *Review of Scientific Instruments* **68**, 3277–3295 (1997).
32. Collier, J., Hernandez-Gomez, C., Allott, R., Danson, C. & Hall, A. A single-shot third-order autocorrelator for pulse contrast and pulse shape measurements. *Laser and Particle Beams* **19**, 231–235 (2001).
33. Gabolde, P. & Trebino, R. Single-frame measurement of the complete spatiotemporal intensity and phase of ultrashort laser pulses using wavelength-multiplexed digital holography. *Journal of the Optical Society of America B* **25**, A25 (2008).
34. Nakagawa, K. *et al.* Sequentially timed all-optical mapping photography (STAMP). *Nature Photonics* **8**, 695–700 (2014).
35. Siders, C. W., Siders, J. L. W., Taylor, A. J., Park, S.-G. & Weiner, A. M. Efficient high-energy pulse-train generation using a 2n-pulse michelson interferometer. *Applied Optics* **37**, 5302 (1998).
36. Kaluza, M. C., Santala, M. I. K., Schreiber, J., Tsakiris, G. D. & Witte, K. J. Time-sequence imaging of relativistic laser–plasma interactions using a novel two-color probe pulse. *Applied Physics B* **92**, 475–479 (2008).
37. Green, J. S. *et al.* Single shot, temporally and spatially resolved measurements of fast electron dynamics using a chirped optical probe. *Journal of Instrumentation* **9**, P03003–P03003 (2014).
38. Davidson, Z. E. *et al.* An optically multiplexed single-shot time-resolved probe of laser–plasma dynamics. *Optics Express* **27**, 4416 (2019).
39. Palaniyappan, S. *et al.* Dynamics of relativistic transparency and optical shuttering in expanding overdense plasmas. *Nature Physics* **8**, 763–769 (2012).
40. Hora, H. Theory of relativistic self-focusing of laser radiation in plasmas. *Journal of the Optical Society of America* **65**, 882 (1975).
41. Watts, I. *et al.* Measurements of relativistic self-phase-modulation in plasma. *Physical Review E* **66** (2002).
42. Martinolli, E. *et al.* Fast electron heating of a solid target in ultrahigh-intensity laser pulse interaction. *Physical Review E* **70** (2004).
43. Metzkes, J. *et al.* Reflective optical probing of laser-driven plasmas at the rear surface of solid targets. *Plasma Physics and Controlled Fusion* **58**, 034012 (2016).
44. Akturk, S., Gu, X., Bowlan, P. & Trebino, R. Spatio-temporal couplings in ultrashort laser pulses. *Journal of Optics* **12**, 093001 (2010).
45. Hornung, M. *et al.* Generation of 25-TW Femtosecond Laser Pulses at 515 nm with Extremely High Temporal Contrast. *Applied Sciences* **5**, 1970–1979 (2015).

46. Chien, C. Y. *et al.* Single-shot chirped-pulse spectral interferometry used to measure the femtosecond ionization dynamics of air. *Optics Letters* **25**, 578 (2000).
47. Le Blanc, S. P., Gaul, E. W., Matlis, N. H., Rundquist, A. & Downer, M. C. Single-shot measurement of temporal phase shifts by frequency-domain holography. *Optics Letters* **25**, 764 (2000).
48. Dromey, B. *et al.* Picosecond metrology of laser-driven proton bursts. *Nature Communications* **7**, 10642 (2016).
49. Scuderi, V. *et al.* Time of Flight based diagnostics for high energy laser driven ion beams. *Journal of Instrumentation* **12**, C03086–C03086 (2017).
50. Morgan, C. G. Laser-induced breakdown of gases. *Reports on Progress in Physics* **38**, 621–665 (1975).
51. Stuart, B. C. *et al.* Nanosecond-to-femtosecond laser-induced breakdown in dielectrics. *Physical Review B* **53**, 1749–1761 (1996).
52. Soong, K., Colby, E. R. & McGuinness, C. Experimental Determination of Damage Threshold Characteristics of IR Compatible Optical Materials. *New York* **3** (2011).
53. Zhokhov, P. A. & Zheltikov, A. M. Optical breakdown of solids by few-cycle laser pulses. *Scientific Reports* **8** (2018).
54. Austin, D. R. *et al.* Femtosecond laser damage of germanium from near- to mid-infrared wavelengths. *Optics Letters* **43**, 3702 (2018).

Acknowledgements

The DFG-funded Cluster of Excellence Munich-Centre for Advanced Photonics (MAP) supported this work. We want to thank Prof. Stefan Karsch and his great team, Max Gilljohann, Hao Ding, Johannes Goetzfried, Gregor Schilling, Sabine Schindler for their tremendous effort in building, operating and improving the ATLAS-300 laser. We also want to thank Peter Hilz, Matthias Otto Haug, Daniel Hahner, Sebastian Seufferling, Jerzy Szerypo and Simon Storck for excellent support concerning the plasma targets. We also want to thank Paul Bolton for excellent support composing the manuscript.

Author Contributions

T.M.O., C.K. and D.H. designed and built the experimental infrastructure in LEX-Photonics. D.H., M.S. and J.H.B. designed and built the experimental infrastructure. K.A. and J.S. developed the idea and first tests for the multi-frame imaging technique. D.H., M.S., J.H.B., J.H. and E.R. performed the experiments. D.H., M.S., J.H.B. and J.S. analyzed the data, discussed and interpreted the results and prepared the manuscript.

Additional Information

Competing Interests: The authors declare no competing interests.

Publisher's note: Springer Nature remains neutral with regard to jurisdictional claims in published maps and institutional affiliations.



Open Access This article is licensed under a Creative Commons Attribution 4.0 International License, which permits use, sharing, adaptation, distribution and reproduction in any medium or format, as long as you give appropriate credit to the original author(s) and the source, provide a link to the Creative Commons license, and indicate if changes were made. The images or other third party material in this article are included in the article's Creative Commons license, unless indicated otherwise in a credit line to the material. If material is not included in the article's Creative Commons license and your intended use is not permitted by statutory regulation or exceeds the permitted use, you will need to obtain permission directly from the copyright holder. To view a copy of this license, visit <http://creativecommons.org/licenses/by/4.0/>.

© The Author(s) 2019